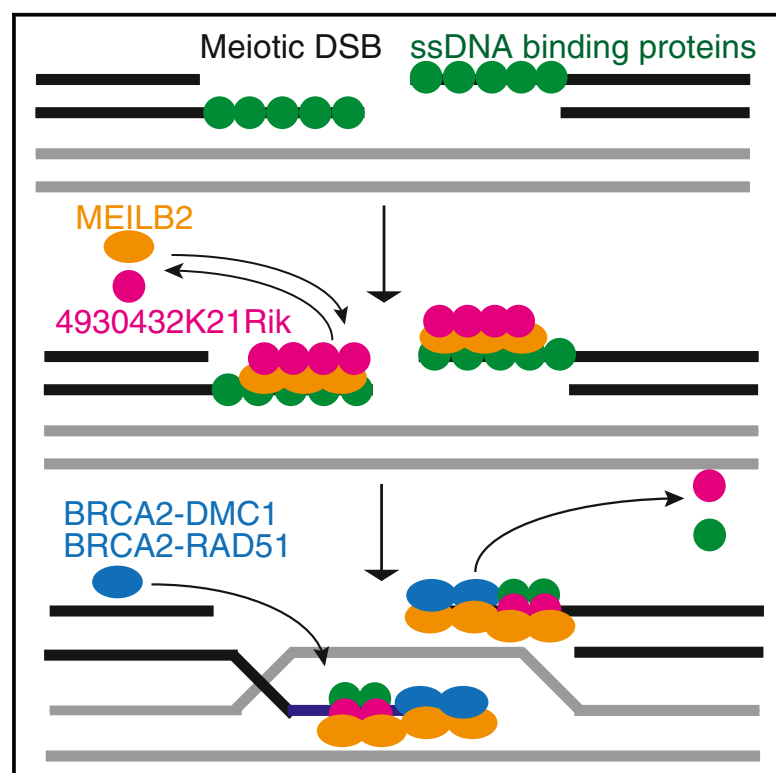


Meiosis-Specific C19orf57/4930432K21Rik/BRME1 Modulates Localization of RAD51 and DMC1 to DSBs in Mouse Meiotic Recombination

Graphical Abstract



Authors

Kazumasa Takemoto, Naoki Tani, Yuki Takada-Horisawa, ..., Michihiko Sugimoto, Kimi Araki, Kei-ichiro Ishiguro

Correspondence

ishiguro@kumamoto-u.ac.jp

In Brief

Meiotic recombination is critical for genetic exchange and chiasmata generation. For this process, recombinases must localize to DNA double-strand breaks (DSBs). Takemoto et al. identify 4930432K21Rik/BRME1 as a loader of recombinases (RAD51 and DMC1) onto DSB sites through the interaction with single-stranded DNA (ssDNA) binding proteins, BRCA2 and MEILB2/HSF2BP, during meiotic recombination.

Highlights

- 4930432K21Rik/BRME1 is a player for meiotic recombination in mice
- 4930432K21Rik/BRME1 associates with ssDNA binding proteins, BRCA2 and MEILB2/HSF2BP
- Disruption of 4930432K21Rik/BRME1 shows severe impact on DSB repair and male fertility
- 4930432K21Rik/BRME1 modulates the localization of RAD51 and DMC1 to meiotic DSB sites



Report

Meiosis-Specific C19orf57/4930432K21Rik/BRME1 Modulates Localization of RAD51 and DMC1 to DSBs in Mouse Meiotic Recombination

Kazumasa Takemoto,^{1,2} Naoki Tani,³ Yuki Takada-Horisawa,¹ Sayoko Fujimura,³ Nobuhiro Tanno,¹ Mariko Yamane,⁵ Kaho Okamura,¹ Michihiko Sugimoto,² Kimi Araki,^{2,4} and Kei-ichiro Ishiguro^{1,6,*}

¹Department of Chromosome Biology, Institute of Molecular Embryology and Genetics (IMEG), Kumamoto University, Kumamoto 860-0811, Japan

²Institute of Resource Development and Analysis, Kumamoto University, Kumamoto 860-0811, Japan

³Liaison Laboratory Research Promotion Center, IMEG, Kumamoto University, Kumamoto 860-0811, Japan

⁴Center for Metabolic Regulation of Healthy Aging, Kumamoto University, Kumamoto 860-0811, Japan

⁵RIKEN, Center for Biosystems Dynamics Research, Kobe 650-0047, Japan

⁶Lead Contact

*Correspondence: ishiguro@kumamoto-u.ac.jp

<https://doi.org/10.1016/j.celrep.2020.107686>

SUMMARY

Meiotic recombination is critical for genetic exchange and generation of chiasmata that ensures faithful chromosome segregation during meiosis I. Meiotic recombination is initiated by DNA double-strand break (DSB) followed by multiple processes of DNA repair. The exact mechanisms for how recombinases localize to DSB remain elusive. Here, we show that C19orf57/4930432K21Rik/BRME1 is a player for meiotic recombination in mice. C19orf57/4930432K21Rik/BRME1 associates with single-stranded DNA (ssDNA) binding proteins, BRCA2 and MEILB2/HSF2BP, which are critical recruiters of recombinases onto DSB sites. Disruption of C19orf57/4930432K21Rik/BRME1 shows severe impact on DSB repair and male fertility. Remarkably, removal of ssDNA binding proteins from DSB sites is delayed, and reciprocally, the loading of RAD51 and DMC1 onto resected ssDNA is impaired in *Brme1* knockout (KO) spermatocytes. We propose that C19orf57/4930432K21Rik/BRME1 modulates localization of recombinases to meiotic DSB sites through the interaction with the BRCA2-MEILB2/HSF2BP complex during meiotic recombination.

INTRODUCTION

Meiosis consists of a single DNA replication followed by two rounds of chromosome segregation (meiosis I and meiosis II), which halves the chromosome number to ultimately produce haploid gametes. During meiotic prophase I, sister chromatids are organized into proteinaceous structures, termed axial element (AE) or chromosome axis (Zickler and Kleckner, 2015). Homologous chromosomes (homologs) then undergo synapsis, which is promoted by assembly of the synaptonemal complex (SC) (Cahoon and Hawley, 2016; Gerton and Hawley, 2005; Page and Hawley, 2004), and meiotic recombination yielding crossovers (COs), a process that produces physical linkages between homologs called chiasmata.

Meiotic recombination is initiated by the introduction of double-strand break (DSB) (Lam and Keeney, 2014; Baudat et al., 2013) by SPO11 (Baudat et al., 2000; Romanienko and Camerini-Otero, 2000) and TOPO6BL (Robert et al., 2016; Vrielynck et al., 2016), and is completed by subsequent homologous recombination (HR)-mediated repair using homologs instead of sister chromatids as a template (Baudat and de Massy, 2007; Handel and Schimenti, 2010; Neale and Keeney, 2006). DNA-

ends at DSBs are resected to form 3'-extended single-stranded DNA (ssDNA) for invasion into a homologous template. ssDNA is coated by multiple ssDNA binding proteins, replication protein A (RPA) complexes (RPA1, RPA2, and RPA3) (Wold et al., 1998; Ribeiro et al., 2016), MEIOB (Luo et al., 2013; Souquet et al., 2013), and SPATA22 (Ishishita et al., 2014; La Salle et al., 2012; Xu et al., 2017), to prevent degradation and secondary structure formation. Subsequently, RAD51 and DMC1 promote preceding removal of ssDNA binding proteins from ssDNA and facilitate invasion of 3'-extended strand into the duplex of the homolog (Cloud et al., 2012; Kurzbauer et al., 2012; Shinohara and Shinohara, 2004). In plants and mammals, BRCA2 directly interacts with RAD51 and DMC1, and plays an essential role in loading them onto ssDNA-ends (Jensen et al., 2010; Sharan et al., 2004; Sliad et al., 2004). Furthermore, recruitment of RAD51 and DMC1 on ssDNA is mediated by MEILB2/HSF2BP through the interaction with BRCA2 (Brandsma et al., 2019; Zhang et al., 2019). Although it has been proposed that MEILB2/HSF2BP-BRCA2 interaction plays a crucial role in the recruitment of RAD51 and DMC1 onto ssDNA, the exact mechanisms for how the MEILB2/HSF2BP-BRCA2 complex acts for ssDNA processing remain elusive (Zhang et al., 2019).



Previously, we identified that MEIOSIN plays an essential role in meiotic initiation both in males and in females (Ishiguro et al., 2020). MEIOSIN, together with STRA8, acts as a crucial transcription factor to drive meiotic gene activation. 4930432K21Rik gene was identified as one of the MEIOSIN/STRA8-regulated genes, whose expression was significantly downregulated in RNA sequencing (RNA-seq) analysis of *Meiosin* knockout (KO) (Ishiguro et al., 2020). And now, here we show that 4930432K21Rik, which we refer to as BRCA2 and MEILB2-associated protein 1 (BRME1), is a meiotic recombination factor that modulates the loading of DMC1 and RAD51. We showed that BRME1 interacts with MEILB2/HSF2BP and BRCA2. Disruption of *Brme1* leads to defects in DSB repair and homolog synapsis, with severe impact on male fertility. In the absence of BRME1, removal of ssDNA binding proteins at the resected DNA-ends was delayed, and reciprocal recruitment of DMC1 and RAD51 was impaired during meiotic recombination. The present study suggests that BRME1 facilitates the recruitment of DMC1 and RAD51 to meiotic DSB sites through interaction with the BRCA2-MEILB2/HSF2BP complex during meiotic recombination.

RESULTS

C19orf57/BRME1 Localizes along the Chromosome Axis during Meiotic Prophase

A previously uncharacterized 4930432K21Rik gene was identified as one of the MEIOSIN/STRA8-bound genes during preleptotene (Figure S1A), whose expression was significantly downregulated in RNA-seq analysis of *Meiosin* KO (Ishiguro et al., 2020). Indeed, RT-PCR analysis demonstrated that 4930432K21Rik expression level was downregulated in *Meiosin* KO testis compared with post-natal day 10 (P10) wild-type (WT) testes, where a cohort of spermatocytes undergoes the first wave of meiotic entry (Figure S1B).

We further examined the expression pattern of the 4930432K21Rik in different mouse tissues using RT-PCR analysis. The 4930432K21Rik gene showed a specific expression in adult testis and embryonic ovary, but not in other adult organs that we examined (Figures 1A and 1B), suggesting that 4930432K21Rik is a germ-cell-specific factor. Public RNA-seq data of human cancer cells (Tang et al., 2017) indicated that human 4930432K21Rik homolog was expressed not only in testis, but also in human tumors such as brain lower-grade glioma, ovarian serous cystadenocarcinoma, and thymoma (Figure S1C; see also Discussion). Mouse 4930432K21Rik gene encodes a hypothetical protein C19orf57 homolog that possesses a conserved domain of unknown function (DUF4671). BLAST search analysis revealed that C19orf57 is conserved in vertebrates (Figure S2). After its biological function described below, we referred to the protein product C19orf57 encoded by 4930432K21Rik gene as the BRME1. To examine the subcellular localization patterns of this hypothetical protein, we immunostained spread chromosomes of spermatocytes with specific antibodies against BRME1, along with SYCP3 (a component of meiotic AE) and SYCP1 (a marker of homolog synapsis). The results showed that BRME1 protein appeared as foci along the chromosomes (Figure 1C). BRME1 foci faintly appeared on the

nuclei at leptotene stage. Subsequently, the number of those foci culminated with more intense signals at zygotene and declined from pachytene stage onward, with residual foci persisting at diplotene. BRME1 foci were absent in *Spo11* KO spermatocytes (Figure 1D), whose DSB formation is defective (Lam and Keeney, 2014; Baudat et al., 2013), indicating nuclear localization of BRME1 depends on DSBs. Notably, BRME1 foci were observed along unsynapsed axes, further implying its role at recombination nodules (Figure 1C). It should be mentioned that BRME1 foci showed less intense signals along synapsed chromosome, suggesting that BRME1 dissociated after homolog synapsis. Similarly, BRME1 protein appeared as foci in embryonic oocytes in a similar manner as spermatocytes, albeit faint signals (Figure S4A). The observed spatiotemporal localization pattern of BRME1 protein resembled those of the factors involved in meiotic recombination, implying that BRME1 plays a role in the process of DSB repair during meiotic recombination.

Disruption of *Brme1* Led to Severe Defect in Spermatogenesis

In order to address the role of *Brme1*/4930432K21Rik in meiosis, we deleted exons 3–9 of *Brme1*/4930432K21Rik loci in C57BL/6 fertilized eggs through the CRISPR-Cas9 system (Figure 2A). Western blotting of the extract from *Brme1* KO testis showed that BRME1 protein was absent (Figure 2B), and immunolocalization of BRME1 along the chromosomes was diminished in *Brme1* KO (Figure 2C), indicating that the targeted *Brme1*/4930432K21Rik allele was null. Although *Brme1* KO male mice did not show overt phenotype in somatic tissues, defects in male reproductive organs were evident with smaller-than-normal testes (Figure 2D). Histological analysis revealed that the diameters of seminiferous tubules were reduced compared with those of WT or heterozygous mice, with slight residual presence of post-meiotic spermatids or sperms in a subpopulation of the tubules (59.8% of total tubules) in 8-week-old *Brme1* KO testes (Figure S3A). Close inspection of seminiferous tubules indicated that some, if any, seminiferous tubules of *Brme1* KO testis contained only a limited number of post-meiotic spermatids and sperms (Figure S3A). Flow cytometry analysis of propidium iodide (PI)-stained testicular cells isolated from 8-week-old WT, *Brme1*^{+/-}, and *Brme1* KO mice showed that a smaller population of 1N haploid cells was produced in *Brme1* KO mice compared with the control littermate (37.6% of 1N haploid cells in WT, 42.2% in *Brme1*^{+/-}, and 15.1% in *Brme1* KO testicular cells) (Figure S3B). Accordingly, the sperm density was largely reduced in *Brme1* KO caudal epididymis compared with those of the WT and *Brme1*^{+/-} littermates (Figure S3C). Mice heterozygous for the *Brme1* allele showed no obvious difference from WT (*Brme1*^{+/+}) in fertility and histology in testes. To examine whether *Brme1* KO affected male fertility, we mated mature *Brme1* KO males and their control littermates with WT females over a period of 5–6 months. Whereas the control males produced a normal size of litters over this period, the *Brme1* KO males showed significantly reduced fertility (Figure S3D). In contrast with males, *Brme1* KO females exhibited seemingly normal fertility with no apparent defect in adult ovaries (Figures S3D and S4B).

We further investigated the fate of *Brme1* KO spermatocytes. Testis-specific histone H1t is a marker of spermatocytes later

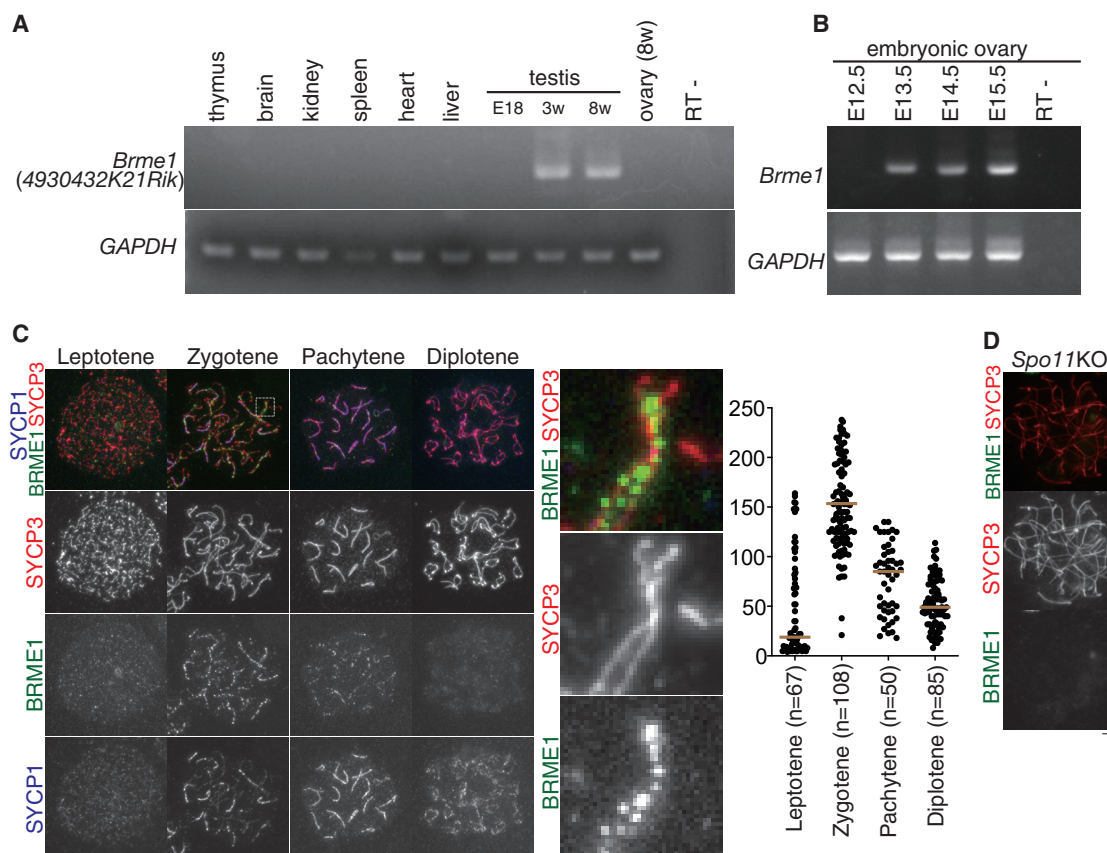


Figure 1. Identification of the Meiosis-Specific Factor C19orf57/4930432K21Rik/BRME1

(A) The tissue-specific expression pattern of 4930432K21Rik/*Brme1* was examined using RT-PCR. Testis RNA was obtained from embryonic day 18 (E18.5) testis and tissues from adult 8-week-old male mice.

(B) The expression pattern of 4930432K21Rik/*Brme1* in the embryonic ovary was examined using RT-PCR. Ovary RNA was obtained from E12.5–E15.5 female mice.

(C) Chromosome spreads of WT spermatocytes were stained for BRME1, SYCP3, and SYCP1. Enlarged images are shown to highlight axes that are going to be synapsed (middle). Numbers of BRME1 foci on SYCP3 axes are shown in the scatterplot with median (right). n indicates the number of cells examined. For immunostaining background, BRME1-immunostained signals were counted in *Brme1* KO. Note that the numbers of BRME1 foci were significantly high in WT compared with those in *Brme1* KO (see Figure 2C).

(D) Chromosome spreads of *Spo11* KO spermatocytes were stained for BRME1 and SYCP3.

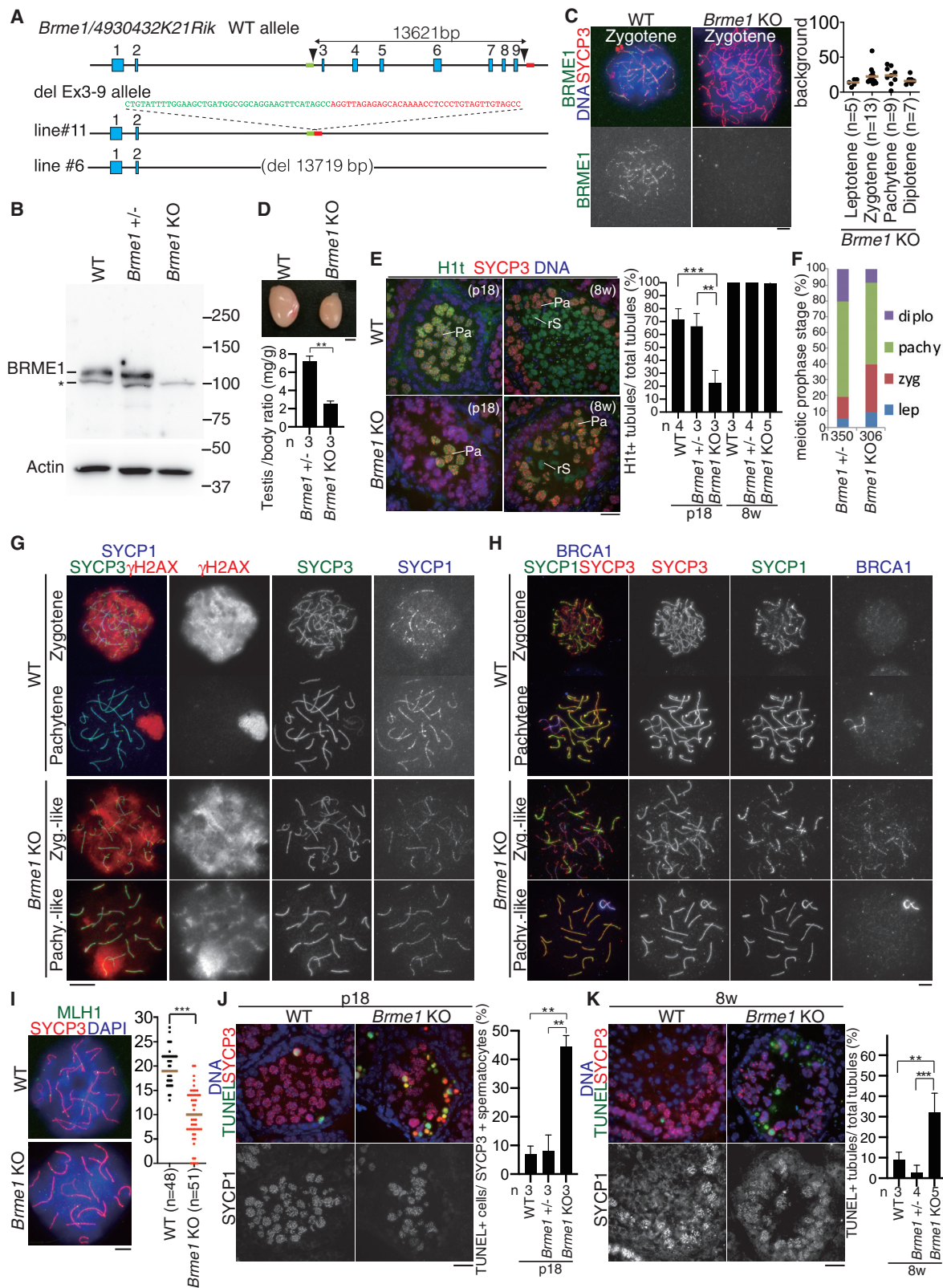
Scale bars, 5 μ m. RT–, control PCR without reverse transcription.

than mid-pachytene. Immunostaining of seminiferous tubules by testis-specific histone H1t indicated that *Brme1* KO spermatocytes reached at least mid to late pachytene stage at P18, whereas the first wave of spermatogenesis had reached late pachytene stage in WT (Figure 2E). However, we noticed that the H1t-positive population was markedly reduced in *Brme1* KO testes compared with WT and heterozygous controls at P18 (Figure 2E), suggesting that progression of meiotic prophase was delayed or blocked in *Brme1* KO spermatocytes. Furthermore, counting the meiotic prophase population indicated that pachytene and diplotene populations were markedly reduced in *Brme1* KO spermatocytes (60.5% versus 51.6% in pachytene, 20.2% versus 8.4% in diplotene for control and *Brme1* KO, respectively) (Figure 2F). Accordingly, the zygotene population apparently accumulated in *Brme1* KO spermatocytes (14.0% versus 30.3% for control and *Brme1* KO, respectively), suggesting that progression of meiotic prophase was compromised

without BRME1. Therefore, although *Brme1* was not necessarily required for fertility in females, its absence had a severe impact on male fertility.

Brme1 KO Spermatocytes Show Defects in DSB Repair

DSB formation and repair are essential steps in meiotic recombination during meiotic prophase. Aforementioned results suggested that BRME1 protein acts for meiotic recombination (Figure 1C). To determine the primary defect leading to subfertility in *Brme1* KO males, we analyzed the progression of meiotic prophase in *Brme1* KO testes. We examined DSB formation and repair events using immunostaining of γ H2AX. A first wave of γ H2AX is mediated by ATM after DSB formation at leptotene (Mahadevaiah et al., 2001) and disappears during DSB repair. The second wave of γ H2AX at zygotene is mediated by ATR that targets unsynapsed chromosomes (Royo et al., 2013). At leptotene and zygotene, γ H2AX signal appeared in *Brme1* KO



(legend on next page)

spermatocytes in the same manner as WT (Figure 2G), indicating that DSB formation normally occurred in *Brme1* KO spermatocytes. However, we noticed that γ H2AX signals largely persisted throughout the nuclei until the pachytene-like stage in *Brme1* KO spermatocytes, whereas they overall disappeared in WT pachytene spermatocytes except retaining on the XY body (Figure 2G). This observation suggested that DSB repair was delayed or blocked in *Brme1* KO spermatocytes. Furthermore, BRCA1, a marker of asynapsis (Scully et al., 1997; Broering et al., 2014), persisted along unsynapsed autosomal axes in zygotene-like *Brme1* KO spermatocytes (Figure 2H), suggesting that meiotic silencing of unsynapsed chromatin (MUSC) was activated as a result of delayed homolog synapsis in *Brme1* KO spermatocytes. A subpopulation of *Brme1* KO spermatocytes indeed showed a pachytene morphology, whose 19 pairs of autosomal axes were apparently fully synapsed. However, the number of MLH1 foci, a marker of CO, was significantly reduced in *Brme1* KO pachytene-like spermatocytes compared with WT pachytene spermatocytes (Figure 2I). This implies that CO recombination was incomplete or delayed in the absence of BRME1, despite the fact that a subpopulation of *Brme1* KO spermatocytes reached mid to late pachytene stage (Figure 2E).

Consequently, TUNEL-positive cells were robustly observed in the *Brme1* KO tubules (average 44.3% of TUNEL-positive spermatocytes in a given tubule) at P18, when the first wave of meiotic prophase reached late pachytene (Figure 2J). The same phenotype persisted through adulthood in *Brme1* KO testes, because a higher number of the TUNEL-positive seminiferous tubules (~31.9%) was observed in *Brme1* KO testis (Fig-

ure 2K). TUNEL-positive cells were exclusively observed in the seminiferous tubules that contained pachytene spermatocytes (Figures 2J and 2K), and the H1t-positive population was reduced in *Brme1* KO testes compared with the controls at P18 (Figure 2E). These observations suggested that a certain population of *Brme1* KO spermatocytes was consequently eliminated by apoptosis, probably leading to stage IV arrest. As a result, *Brme1* KO testes showed seminiferous tubules lacking post-meiotic spermatids or sperms at 8 weeks old (Figure S3A). Therefore, we reasoned that the primary defect in *Brme1* KO testes derived from failure of DSB repair during meiotic prophase.

BRME1 Facilitates Recruitment of RAD51 and DMC1 Recombinases to DSB Sites

Given that BRME1 is required for DSB repair, we sought how BRME1 was involved in DSB repair processes by screening its interacting factors. Mass spectrometry (MS) analysis of immunoprecipitates of BRME1 from testes extracts identified MEILB2/HSF2BP (Brandsma et al., 2019; Yoshima et al., 1998; Zhang et al., 2019), BRCA2 (Sharan et al., 2004), RPA1 (Wold et al., 1998), and MEIOB (Luo et al., 2013; Souquet et al., 2013), which are known to play a role in meiotic recombination (Figure 3A; Table S2). Immunoprecipitation (IP) followed by western blotting using testes extracts indicated that BRME1 indeed coprecipitated those factors (Figure 3B). This suggests that BRME1 mediates the process of meiotic recombination through the interaction with these factors. Notably, it was shown that MEILB2/HSF2BP directly interacts with BRCA2 and plays a

Figure 2. *Brme1* KO Spermatocytes Show Defects in DSB Repair and Homolog Synapsis

- (A) The targeted exons 3–9 deletion allele of *Brme1* was generated by the introduction of CAS9, the synthetic guide RNAs (gRNAs) designed to target intron 2 and the downstream of exon 9 (arrowheads), and single-stranded oligodeoxynucleotide (ssODN) into C57BL/6 fertilized eggs. Two lines of KO mice were established. Line 11 of *Brme1* KO mice was used in most of the experiments, unless otherwise stated.
- (B) Immunoblot analysis of testis extracts prepared from WT, *Brme1*^{+/−}, and *Brme1* KO mice (P18). Note that BRME1 protein migrated slower than the expected size calculated from the molecular weight. Asterisk (*) indicates a non-specific band.
- (C) Chromosome spreads of WT and *Brme1* KO spermatocytes were stained for BRME1, SYCP3, and DAPI. Numbers of background BRME1-immunostained signals in *Brme1* KO axes are shown in the scatterplot with median (right). n indicates the number of cells examined. Note that the BRME1-immunostained signals in *Brme1* KO were considered to be background, and their numbers were negligibly small compared with those in WT as shown in Figure 1C, confirming the specificity of the anti-BRME1 antibody. Scale bar, 5 μ m.
- (D) Testes from WT and *Brme1* KO mice (8 weeks old [8w]). Scale bar, 2 mm. Testis/body weight ratio (mg/g) of *Brme1*^{+/−} and *Brme1* KO mice (8w). n, number of animals examined. Statistical significance is shown by p values (paired t test). **p < 0.01.
- (E) Seminiferous tubule sections from WT and *Brme1* KO mice (P18, 8w) were stained as indicated. Shown below is the quantification of the seminiferous tubules that have H1t⁺/SYCP3⁺ cells per the seminiferous tubules that have SYCP3⁺ spermatocyte cells in WT (P18: n = 4, 8w: n = 3), heterozygous (P18: n = 3, 8w: n = 4), and *Brme1* KO (P18: n = 3, 8w: n = 5) testes (bar graph with SD). n, the number of animals examined for each genotype. Statistical significance is shown by p value (t test). **p < 0.01, ***p < 0.001. Scale bar, 25 μ m.
- (F) Chromosome spreads of *Brme1*^{+/−} and *Brme1* KO spermatocytes (P20) were stained as indicated. Cells in the four developmental stages (leptotene, zygotene, pachytene, and diplotene) were quantified in WT and *Brme1* KO. n, number of animals examined.
- (G) Chromosome spreads of WT and *Brme1* KO spermatocytes were stained as indicated.
- (H) Chromosome spreads of WT and *Brme1* KO spermatocytes were stained as indicated.
- (I) Chromosome spreads of WT and *Brme1* KO spermatocytes were stained for MLH1, SYCP3, and DAPI. Statistical significance is shown by p value (Mann-Whitney U test). ***p < 0.0001. Scale bars, 5 μ m.
- (J) Seminiferous tubule sections from WT, *Brme1*^{+/−}, and *Brme1* KO mice (P18) were stained as indicated. Shown on the right is the quantification of the TUNEL⁺ cells per total SYCP3⁺ spermatocytes. Percentages of TUNEL⁺ cells were calculated in 16 seminiferous tubules that have at least one TUNEL⁺ cell. Averaged percentage from three animals (total of 48 tubules) for each genotype is shown with SD. Statistical significance is shown by p values (paired t test). **p < 0.01. Scale bar, 25 μ m.
- (K) Seminiferous tubule sections from 8w mice were immunostained as in (I). Shown on the right is the quantification of the seminiferous tubules that have TUNEL⁺ cells per total tubules in WT (8w: n = 3), *Brme1*^{+/−} (8w: n = 4), and *Brme1* KO (8w: n = 5) testes (bar graph with SD). Statistical significance is shown by p values (paired t test). **p < 0.01, ***p < 0.001. Scale bar, 25 μ m.
- diplotene; eS, elongated spermatid; lep, leptotene; Pa, pachytene spermatocyte; pachy, pachytene; Pachy.-like: pachytene-like; rS, round spermatid; zyg, zygotene; Zyg.-like, zygotene-like.

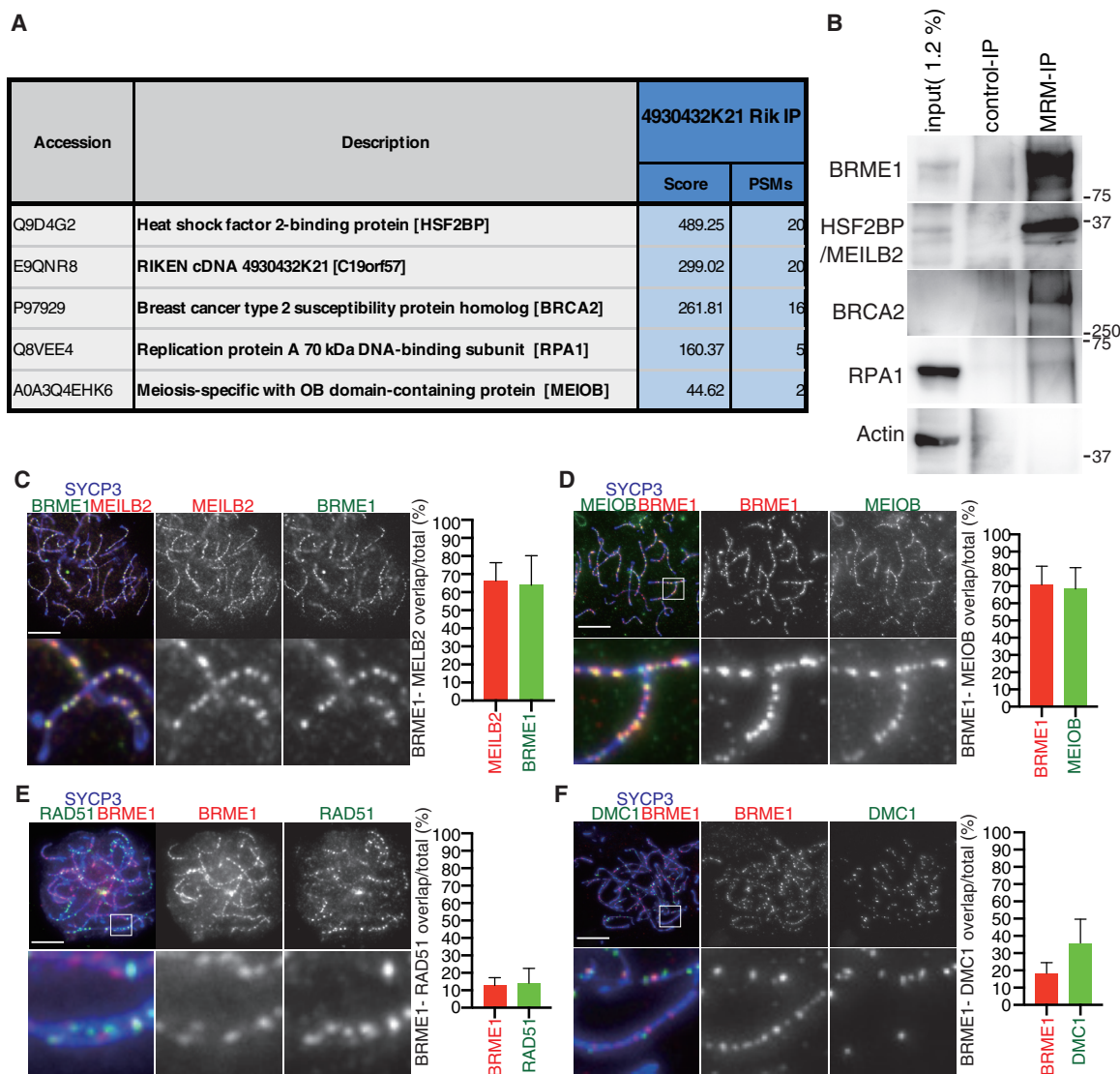


Figure 3. BRME1 Interacts with BRCA2, MEILB2, and ssDNA Binding Proteins

Figure360> For a Figure360 author presentation of this figure, see <https://doi.org/10.1016/j.celrep.2020.107686>.

(A) The immunoprecipitates of BRME1 from the chromatin-unbound fraction of the testis (P18) were subjected to liquid chromatography tandem-mass spectrometry (LC-MS/MS) analyses. The meiotic recombination proteins identified in the LC-MS/MS analyses of the samples are listed with the number of peptide hits and Mascot scores in the table. See Table S2 for a full list of raw MS/MS data.

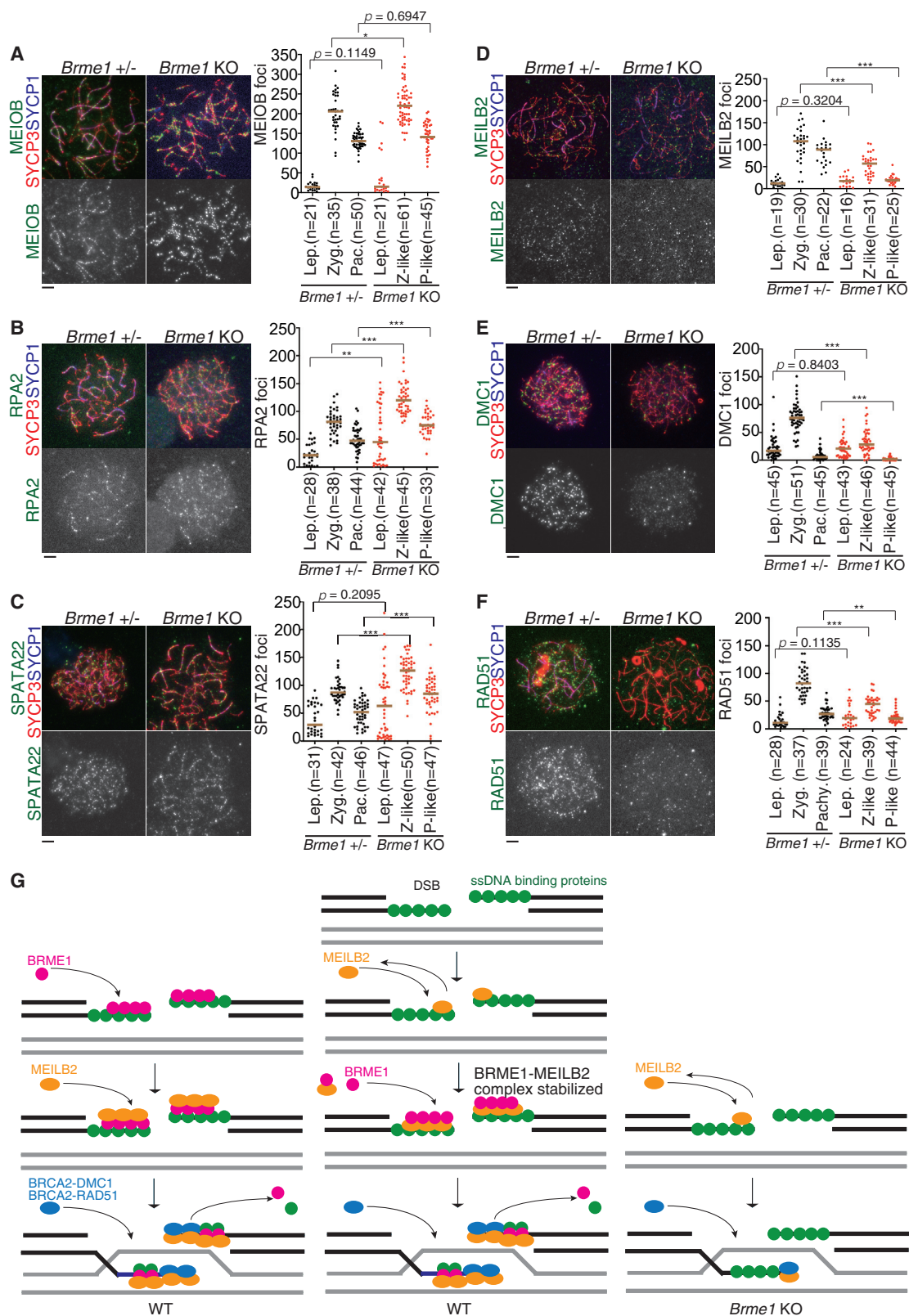
(B) Immunoprecipitates of BRME1 from chromatin-unbound extracts of WT testes were immunoblotted as indicated.

(C–F) Chromosome spreads of WT zygotene spermatocytes were stained as indicated. Scale bars, 5 μ m. (C) Quantification of overlapped BRME1 and MEILB2 foci per total BRME1 or per total MEILB2 is shown ($n = 10$). (D) Quantification of overlapped BRME1 and MEIOB foci per total BRME1 or per total MEIOB is shown ($n = 11$). (E) Quantification of overlapped BRME1 and RAD51 foci per total BRME1 or per total RAD51 is shown ($n = 15$). (F) Quantification of overlapped BRME1 and DMC1 foci per total BRME1 or per total DMC1 is shown ($n = 11$).

role in recruiting recombinase RAD51 to DSBs through the interaction between BRCA2 and RAD51 (Zhang et al., 2019). Indeed, BRME1 overall colocalizes with MEILB2/HSF2BP and MEIOB on the chromatin at zygotene (Figures 3C and 3D), although it rarely did with RAD51 and DMC1 (Figures 3E and 3F).

We further monitored the dynamics of those factors involved in meiotic recombination in *Brme1* KO. Following DSB introduction, ssDNA binding proteins, RPA1, RPA2, RPA3 (Ribeiro et al., 2016), SPATA22 (Ishishita et al., 2014; La Salle et al.,

2012; Xu et al., 2017), and MEIOB (Luo et al., 2013; Souquet et al., 2013), localize to the resected ssDNA-ends. Subsequently, DMC1 and RAD51 are recruited to the DNA-ends to promote strand invasion for HR (Pittman et al., 1998; Yoshida et al., 1998; Cloud et al., 2012). In WT spermatocytes, ssDNA binding proteins, RPA2, MEIOB, and SPATA22, appeared at leptotene, culminated at zygotene, and declined toward pachytene as the resected ssDNA were repaired (Figures 4A–4C). In contrast, an elevated number of RPA2 and SPATA22 foci were accumulated



(legend on next page)

in *Brme1* KO spermatocytes compared with the controls (Figures 4B and 4C), suggesting that the removal of RPA2 and SPATA22 was delayed or impaired in the absence of BRME1. We noticed that whereas an elevated number of MEIOB foci were accumulated at zygotene in *Brme1* KO spermatocytes, a comparable number of MEIOB foci were observed at pachytene in the control and *BRME1* KO spermatocytes (Figure 4A). Because MEIOB rather persisted along the axes at pachytene irrespective of the presence or absence of BRME1 (Figure 4A), MEIOB may have another role in the processing of joint molecules at a later stage of recombination as proposed in the previous study (Luo et al., 2013).

Crucially, localization of MEILB2/HSF2BP was partly impaired in *Brme1* KO spermatocytes (Figure 4D), suggesting that BRME1 facilitates localization of MEILB2/HSF2BP onto DSB sites or stabilizes MEILB2/HSF2BP on resected ssDNA. Accordingly, the number of RAD51 and DMC1 foci was significantly reduced in *Brme1* KO spermatocytes (Figures 4E and 4F), suggesting that localization of RAD51 and DMC1 was partly destabilized or delayed in the absence of BRME1. However, *Brme1* KO showed less impact on localization of RAD51 and DMC1 than *Meilb2* KO, whereas RAD51 and DMC1 were completely abolished (Zhang et al., 2019). These results suggest that BRME1 at least in part facilitates recruitment of RAD51 and DMC1 recombinases to DSB sites through the interaction with MEILB2/HSF2BP and removes ssDNA binding proteins during meiotic recombination (Figure 4G).

DISCUSSION

The present study revealed that BRME1/C19ORF57 plays a role in meiotic recombination. A key finding is that BRME1 interacts with MEILB2/HSF2BP. It has been shown that MEILB2/HSF2BP directly interacts with BRCA2 to promote loading of RAD51 and DMC1 recombinases onto DSB sites (Zhang et al., 2019). This process is mediated by two interactions: between BRCA2 and MEILB2/HSF2BP and between BRCA2 and RAD51/DMC1. However, how MEILB2/HSF2BP localizes to the DSB sites has been unclear. The present study demonstrates that BRME1 interacts with MEILB2/HSF2BP, BRCA2, and ssDNA binding proteins (Figures 3A and 3B). Because armadillo repeats of MEILB2/HSF2BP directly interact with BRCA2 (Brandsma et al., 2019; Zhang et al., 2019), BRCA2 was co-precipitated probably via MEILB2/HSF2BP in our BRME1 immunoprecipitates. BRME1 colocalizes well with MEILB2/HSF2BP and ssDNA binding proteins on the chromatin, while it rarely does with RAD51 and DMC1 (Figures 3C–3F). Furthermore, localizations of ssDNA binding proteins RPA, MEIOB, and SPATA22 were elevated in *Brme1* KO spermatocytes, whereas those of MEILB2/HSF2BP, RAD51, and

DMC1 were partly reduced (Figure 4). These results suggest that BRME1 may initially bind to ssDNA binding proteins and MEILB2/HSF2BP, then facilitate recruitment of the BRCA2-RAD51 and BRCA2-DMC1 complexes onto MEILB2/HSF2BP-bound DSB sites (Figure 4G). Alternatively, MEILB2/HSF2BP associates with resected DSBs, and BRME1 subsequently interacts with MEILB2/HSF2BP, leading to the stabilization of MEILB2/HSF2BP on DSBs. It should be mentioned that removal of the ssDNA binding protein RPA was severely delayed in *Brme1* KO (Figure 4), whereas it was less affected in *Meilb2* KO (Zhang et al., 2019), suggesting that BRME1, rather than MEILB2/HSF2BP, may play a more active role in replacing RPA from ssDNA. Thus, we speculate that BRME1 facilitates the loading of RAD51 and DMC1 recombinases onto DSBs through interaction with MEILB2/HSF2BP and replacing ssDNA binding proteins.

We noticed that BRME1 persisted in the late meiotic prophase (Figure 1C). Further, it was previously shown that MEILB2/HSF2BP persisted in pachytene (Zhang et al., 2019). It was demonstrated that the early meiotic repair pathway that acts by default at the beginning of the meiotic prophase is replaced sequentially by non-homologous end joining (NHEJ) and somatic-like HR pathway involving RAD51 (Enguita-Marruedo et al., 2019). Although we do not yet know the biological relevance of the detectable BRME1 foci in the late meiotic prophase, BRME1 may be involved in the “somatic-like HR repair pathway” in that stage.

In mouse, meiosis-specific ssDNA binding proteins MEIOB (Luo et al., 2013; Souquet et al., 2013) and SPATA22 (Ishishita et al., 2014; La Salle et al., 2012; Xu et al., 2017) exist along with canonical ssDNA binding proteins RPA1–3. Thus, meiosis-specific ssDNA binding proteins have unique roles in processing homology-directed DNA repair during meiotic recombination. It has been shown that MEIOB interacts with SPATA22, and that their chromatin loading is interdependent (Luo et al., 2013). In the present study, we have shown that removal of SPATA22 was affected in *Brme1* KO spermatocytes (Figure 4C), while that of MEIOB apparently was less affected (Figure 4A). We do not know the exact reason for different dynamics of SPATA22 and MEIOB in *Brme1* KO spermatocytes. However, this may be due to the existence of another population of chromatin-bound SPATA22 and MEIOB at different time points, because it was previously proposed that MEIOB might mediate second-end capture after strand invasion (Luo et al., 2013).

DSS1 is widely conserved in vertebrates, nematode, plant, and fungi (Kojic et al., 2003; Marston et al., 1999; Pispas et al., 2008; Dray et al., 2006). In somatic cells, DSS1 interacts with BRCA2 and facilitates RPA-RAD51 exchange on ssDNA during HR (Zhao et al., 2015). Given that DSS1-BRCA2 interaction plays a role in replacing ssDNA binding protein with recombinases at

Figure 4. BRME1 Plays a Role in Recruiting Recombinases onto DSB Sites

(A–F) Chromosome spreads of *Brme1*^{+/+} and *Brme1* KO spermatocytes were stained as indicated. Immunostained chromosome spread of zygotene spermatocytes is shown. Scale bars, 5 μ m. (A) The number of MEIOB foci is shown in the scatterplot with median (right). Statistical significance is shown by p value (Mann-Whitney U test). ***p < 0.0001, **p < 0.001, *p < 0.05. (B) The number of RPA2 foci is shown as in (A). (C) The number of SPATA22 foci is shown as in (A). (D) The number of MEILB2 foci is shown as in (A). (E) The number of DMC1 foci is shown as in (A). (F) The number of RAD51 foci is shown as in (A). (G) Schematic models of the role of BRME1 in meiotic recombination. Two alternative models are shown for WT (left and middle). Putative model is shown for *Brme1* KO (right). In *Brme1* KO, localization of MEILB2 onto DSBs is reduced. Consequently, the localization of recombinases is reduced. Black and gray lines indicate dsDNAs from homologous chromosomes.

Pac., pachytene; P-like, pachytene-like; Z-like, zygotene-like; Zyg., zygotene.

DSBs, a similar mechanism may apply to BRME1-MEILB2/HSF2BP-BRCA2 interactions. As in the case of the previous study on MEILB2/HSF2BP (Zhang et al., 2019), requirement of BRME1 was also sexually dimorphic (Figure S4). Although it is yet to be examined whether DSS1 or other factors compensate BRME1 in meiotic recombination, such redundant mechanisms may account for why residual sperm can be produced in *Brme1* KO males (Figure S3), and BRME1 was not necessarily essential for female fertility (Figure S4).

It should be mentioned that our *Brme1* KO male mice were sub-fertile, whereas those from the other group were completely infertile (Felipe-Medina et al., 2020). Although our *Brme1* KO mice had a larger deletion encompassing exons 3–9 in the *Brme1* locus, which corresponded to almost the entire protein coding sequence, resulting in complete null allele (Figure 2A), those from the other group had 40-bp deletion at exon 6, which was predicted to cause a frameshift mutation. Although we do not know the exact reason for the phenotypic difference, it may be due to the difference in the alleles used in the two studies.

Lastly, it should be mentioned that expression levels of human *HSF2BP* are elevated in some tumors (Zhang et al., 2019; Brandsma et al., 2019). Notably, expression levels of *BRME1/C19ORF57* were also elevated in the similar set of tumors (Figure S1C) (Tang et al., 2017). Therefore, it is possible that both *BRME1/C19ORF57* and *MEILB2/HSF2BP* are co-expressed in a particular type of human tumor. This evidence supports the previously proposed hypothesis that ectopic expression of MEILB2 may perturb the intrinsic BRCA2 function through direct interaction in cancer cells (Zhang et al., 2019). Thus, misexpression of *BRME1/C19ORF57* together with MEILB2 may compromise the function of the BRCA2-RAD51 complex during DNA repair in human cancers.

Altogether, our study will shed light on multiple layers of mechanisms for how recombinases are loaded onto DSB sites in vertebrate meiotic recombination.

STAR★METHODS

Detailed methods are provided in the online version of this paper and include the following:

- KEY RESOURCES TABLE
- RESOURCE AVAILABILITY
 - Lead Contact
 - Materials Availability
 - Data and Code Availability
- EXPERIMENTAL MODEL AND SUBJECT DETAILS
 - Animals
- METHOD DETAILS
 - Generation of 4930432K21Rik/*Brme1* knockout mice and genotyping
 - PCR with reverse transcription
 - Preparation of testis extracts and immunoprecipitation
 - Mass spectrometry
 - Antibodies
 - Histological Analysis
 - Immunostaining of spermatocytes
 - Imaging

- FACS analysis
- ChIP-seq Data and Public RNA-seq data Analysis
- QUANTIFICATION AND STATISTICAL ANALYSIS

SUPPLEMENTAL INFORMATION

Supplemental Information can be found online at <https://doi.org/10.1016/j.celrep.2020.107686>.

ACKNOWLEDGMENTS

The authors thank Kumi Matsuura for technical support of ChIP-seq data reanalysis, Shoko Yamaoka for initial RT-PCR screening, and Drs. Satoshi Namekawa and Marry Ann Handel for provision of antibodies. This work was supported in part by KAKENHI (grants 17H03634, 18K19304, 19H05245, 19H05743, 20H03265, and JP 16H06276 from MEXT, Japan), NIG-JOINT (grant 32A2019), the program of the Joint Usage/IMEG Research Center for Developmental Medicine, Takeda Science Foundation, Yamada Science Foundation, and Ichiro Kanehara Foundation for Medical Science and Medical Care (to K.-i.l.).

AUTHOR CONTRIBUTIONS

K.T. performed most of the experiments. N. Tani performed MS analysis. Y.T.-H. performed the RT-PCR and embryonic gonadal experiments. K.A. and M.S. designed the KO mice. N. Tanno performed flow cytometry. K.O. supported the antibody production. S.F. performed histological analyses. M.Y. performed bioinformatics analyses. K.-i.l. supervised experiments, conducted the study, and wrote the manuscript.

DECLARATION OF INTERESTS

The authors declare no competing interests.

Received: February 13, 2020

Revised: April 16, 2020

Accepted: May 4, 2020

Published: May 26, 2020

REFERENCES

- Baudat, F., and de Massy, B. (2007). Regulating double-stranded DNA break repair towards crossover or non-crossover during mammalian meiosis. *Chromosome Res.* 15, 565–577.
- Baudat, F., Manova, K., Yuen, J.P., Jasin, M., and Keeney, S. (2000). Chromosome synapsis defects and sexually dimorphic meiotic progression in mice lacking Spo11. *Mol. Cell* 6, 989–998.
- Baudat, F., Imai, Y., and de Massy, B. (2013). Meiotic recombination in mammals: localization and regulation. *Nat. Rev. Genet.* 14, 794–806.
- Brandsma, I., Sato, K., van Rossum-Fikkert, S.E., van Vliet, N., Sleddens, E., Reuter, M., Odijk, H., van den Tempel, N., Dekkers, D.H.W., Bezstarosti, K., et al. (2019). HSF2BP Interacts with a Conserved Domain of BRCA2 and Is Required for Mouse Spermatogenesis. *Cell Rep.* 27, 3790–3798.e3.
- Broering, T.J., Alavattam, K.G., Sadreyev, R.I., Ichijima, Y., Kato, Y., Hasegawa, K., Camerini-Otero, R.D., Lee, J.T., Andreassen, P.R., and Namekawa, S.H. (2014). BRCA1 establishes DNA damage signaling and pericentric heterochromatin of the X chromosome in male meiosis. *J. Cell Biol.* 205, 663–675.
- Cahoon, C.K., and Hawley, R.S. (2016). Regulating the construction and demolition of the synaptonemal complex. *Nat. Struct. Mol. Biol.* 23, 369–377.
- Cloud, V., Chan, Y.L., Grubb, J., Budke, B., and Bishop, D.K. (2012). Rad51 is an accessory factor for Dmc1-mediated joint molecule formation during meiosis. *Science* 337, 1222–1225.
- Dray, E., Siaud, N., Dubois, E., and Doutriaux, M.P. (2006). Interaction between Arabidopsis Brca2 and its partners Rad51, Dmc1, and Dss1. *Plant Physiol.* 140, 1059–1069.

- Enguita-Marruedo, A., Martín-Ruiz, M., García, E., Gil-Fernández, A., Parra, M.T., Viera, A., Rufas, J.S., and Page, J. (2019). Transition from a meiotic to a somatic-like DNA damage response during the pachytene stage in mouse meiosis. *PLoS Genet.* **15**, e1007439.
- Felipe-Medina, N., Caburet, S., Sánchez-Sáez, F., Condezo, Y.B., de Rooij, D., Gómez-H, L., García-Valiente, R., Todeschini, A.-L., Duque, P., Sánchez-Martín, M., et al. (2020). A missense in HSF2BP causing Primary Ovarian Insufficiency affects meiotic recombination by its novel interactor C19ORF57/MIDAP. *bioRxiv*. <https://doi.org/10.1101/2020.03.05.978007>.
- Gerton, J.L., and Hawley, R.S. (2005). Homologous chromosome interactions in meiosis: diversity amidst conservation. *Nat. Rev. Genet.* **6**, 477–487.
- Handel, M.A., and Schimenti, J.C. (2010). Genetics of mammalian meiosis: regulation, dynamics and impact on fertility. *Nat. Rev. Genet.* **11**, 124–136.
- Ishiguro, K., Kim, J., Fujiyama-Nakamura, S., Kato, S., and Watanabe, Y. (2011). A new meiosis-specific cohesin complex implicated in the cohesin code for homologous pairing. *EMBO Rep.* **12**, 267–275.
- Ishiguro, K., Kim, J., Shibuya, H., Hernández-Hernández, A., Suzuki, A., Fukagawa, T., Shioi, G., Kiyonari, H., Li, X.C., Schimenti, J., et al. (2014). Meiosis-specific cohesin mediates homolog recognition in mouse spermatocytes. *Genes Dev.* **28**, 594–607.
- Ishiguro, K.I., Matsuura, K., Tani, N., Takeda, N., Usuki, S., Yamane, M., Sugimoto, M., Fujimura, S., Hosokawa, M., Chuma, S., et al. (2020). MEIOSIN Directs the Switch from Mitosis to Meiosis in Mammalian Germ Cells. *Dev. Cell* **52**, 429–445.e10.
- Ishishita, S., Matsuda, Y., and Kitada, K. (2014). Genetic evidence suggests that Spata22 is required for the maintenance of Rad51 foci in mammalian meiosis. *Sci. Rep.* **4**, 6148.
- Jensen, R.B., Carreira, A., and Kowalczykowski, S.C. (2010). Purified human BRCA2 stimulates RAD51-mediated recombination. *Nature* **467**, 678–683.
- Kojic, M., Yang, H., Kostrub, C.F., Pavletich, N.P., and Holloman, W.K. (2003). The BRCA2-interacting protein DSS1 is vital for DNA repair, recombination, and genome stability in *Ustilago maydis*. *Mol. Cell* **12**, 1043–1049.
- Kurzbauer, M.T., Uanschou, C., Chen, D., and Schögelhofer, P. (2012). The recombinases DMC1 and RAD51 are functionally and spatially separated during meiosis in *Arabidopsis*. *Plant Cell* **24**, 2058–2070.
- La Salle, S., Palmer, K., O'Brien, M., Schimenti, J.C., Eppig, J., and Handel, M.A. (2012). Spata22, a novel vertebrate-specific gene, is required for meiotic progress in mouse germ cells. *Biol. Reprod.* **86**, 45.
- Lam, I., and Keeney, S. (2014). Mechanism and regulation of meiotic recombination initiation. *Cold Spring Harb. Perspect. Biol.* **7**, a016634.
- Luo, M., Yang, F., Leu, N.A., Landaiche, J., Handel, M.A., Benavente, R., La Salle, S., and Wang, P.J. (2013). MEIOB exhibits single-stranded DNA-binding and exonuclease activities and is essential for meiotic recombination. *Nat. Commun.* **4**, 2788.
- Mahadevaiah, S.K., Turner, J.M., Baudat, F., Rogakou, E.P., de Boer, P., Blanco-Rodríguez, J., Jasin, M., Keeney, S., Bonner, W.M., and Burgoyne, P.S. (2001). Recombinational DNA double-strand breaks in mice precede synapsis. *Nat. Genet.* **27**, 271–276.
- Marston, N.J., Richards, W.J., Hughes, D., Bertwistle, D., Marshall, C.J., and Ashworth, A. (1999). Interaction between the product of the breast cancer susceptibility gene BRCA2 and DSS1, a protein functionally conserved from yeast to mammals. *Mol. Cell. Biol.* **19**, 4633–4642.
- Neale, M.J., and Keeney, S. (2006). Clarifying the mechanics of DNA strand exchange in meiotic recombination. *Nature* **442**, 153–158.
- Page, S.L., and Hawley, R.S. (2004). The genetics and molecular biology of the synaptonemal complex. *Annu. Rev. Cell Dev. Biol.* **20**, 525–558.
- Peters, A.H., Plug, A.W., van Vugt, M.J., and de Boer, P. (1997). A drying-down technique for the spreading of mammalian meiocytes from the male and female germline. *Chromosome Res.* **5**, 66–68.
- Pispa, J., Palmén, S., Holmberg, C.I., and Jäntti, J. (2008). *C. elegans* dss-1 is functionally conserved and required for oogenesis and larval growth. *BMC Dev. Biol.* **8**, 51.
- Pittman, D.L., Cobb, J., Schimenti, K.J., Wilson, L.A., Cooper, D.M., Brignull, E., Handel, M.A., and Schimenti, J.C. (1998). Meiotic prophase arrest with failure of chromosome synapsis in mice deficient for Dmc1, a germline-specific RecA homolog. *Mol. Cell* **1**, 697–705.
- Ribeiro, J., Abby, E., Livera, G., and Martini, E. (2016). RPA homologs and ssDNA processing during meiotic recombination. *Chromosoma* **125**, 265–276.
- Robert, T., Nore, A., Brun, C., Maffre, C., Crimi, B., Bourbon, H.M., and de Massy, B. (2016). The TopoVIB-Like protein family is required for meiotic DNA double-strand break formation. *Science* **351**, 943–949.
- Romanienko, P.J., and Camerini-Otero, R.D. (2000). The mouse Spo11 gene is required for meiotic chromosome synapsis. *Mol. Cell* **6**, 975–987.
- Royo, H., Prosser, H., Ruzankina, Y., Mahadevaiah, S.K., Cloutier, J.M., Baumann, M., Fukuda, T., Höög, C., Tóth, A., de Rooij, D.G., et al. (2013). ATR acts stage specifically to regulate multiple aspects of mammalian meiotic silencing. *Genes Dev.* **27**, 1484–1494.
- Scully, R., Chen, J., Plug, A., Xiao, Y., Weaver, D., Feunteun, J., Ashley, T., and Livingston, D.M. (1997). Association of BRCA1 with Rad51 in mitotic and meiotic cells. *Cell* **88**, 265–275.
- Sharan, S.K., Pyle, A., Coppola, V., Babus, J., Swaminathan, S., Benedict, J., Swing, D., Martin, B.K., Tessarollo, L., Evans, J.P., et al. (2004). BRCA2 deficiency in mice leads to meiotic impairment and infertility. *Development* **131**, 131–142.
- Shinohara, A., and Shinohara, M. (2004). Roles of RecA homologues Rad51 and Dmc1 during meiotic recombination. *Cytogenet. Genome Res.* **107**, 201–207.
- Siaud, N., Dray, E., Gy, I., Gérard, E., Takvorian, N., and Doutriaux, M.P. (2004). Brca2 is involved in meiosis in *Arabidopsis thaliana* as suggested by its interaction with Dmc1. *EMBO J.* **23**, 1392–1401.
- Souquet, B., Abby, E., Hervé, R., Finsterbusch, F., Tourpin, S., Le Bouffant, R., Duquenne, C., Messiaen, S., Martini, E., Bernardino-Sgherri, J., et al. (2013). MEIOB targets single-strand DNA and is necessary for meiotic recombination. *PLoS Genet.* **9**, e1003784.
- Tang, Z., Li, C., Kang, B., Gao, G., Li, C., and Zhang, Z. (2017). GEPIA: a web server for cancer and normal gene expression profiling and interactive analyses. *Nucleic Acids Res.* **45** (W1), W98–W102.
- Thorvaldsdóttir, H., Robinson, J.T., and Mesirov, J.P. (2013). Integrative Genomics Viewer (IGV): high-performance genomics data visualization and exploration. *Brief Bioinform.* **14**, 178–192.
- Vrielynck, N., Chambon, A., Vezon, D., Pereira, L., Chelysheva, L., De Muyt, A., Mézard, C., Mayer, C., and Grelon, M. (2016). A DNA topoisomerase VI-like complex initiates meiotic recombination. *Science* **351**, 939–943.
- Wold, S., Boye, E., Slater, S., Kleckner, N., and Skarstad, K. (1998). Effects of purified SeqA protein on oriC-dependent DNA replication in vitro. *EMBO J.* **17**, 4158–4165.
- Xu, Y., Greenberg, R.A., Schonbrunn, E., and Wang, P.J. (2017). Meiosis-specific proteins MEIOB and SPATA22 cooperatively associate with the single-stranded DNA-binding replication protein A complex and DNA double-strand breaks. *Biol. Reprod.* **96**, 1096–1104.
- Yoshida, K., Kondoh, G., Matsuda, Y., Habu, T., Nishimune, Y., and Morita, T. (1998). The mouse RecA-like gene Dmc1 is required for homologous chromosome synapsis during meiosis. *Mol. Cell* **1**, 707–718.
- Yoshima, T., Yura, T., and Yanagi, H. (1998). Novel testis-specific protein that interacts with heat shock factor 2. *Gene* **214**, 139–146.
- Zhang, J., Fujiwara, Y., Yamamoto, S., and Shibuya, H. (2019). A meiosis-specific BRCA2 binding protein recruits recombinases to DNA double-strand breaks to ensure homologous recombination. *Nat. Commun.* **10**, 722.
- Zhao, W., Vaithiyalingam, S., San Filippo, J., Maranon, D.G., Jimenez-Sainz, J., Fontenay, G.V., Kwon, Y., Leung, S.G., Lu, L., Jensen, R.B., et al. (2015). Promotion of BRCA2-Dependent Homologous Recombination by DSS1 via RPA Targeting and DNA Mimicry. *Mol. Cell* **59**, 176–187.
- Zickler, D., and Kleckner, N. (2015). Recombination, Pairing, and Synapsis of Homologs during Meiosis. *Cold Spring Harb. Perspect. Biol.* **7**, a016626.

STAR★METHODS

KEY RESOURCES TABLE

REAGENT or RESOURCE	SOURCE	IDENTIFIER
Antibodies		
Rabbit anti-Actin (IF, 1:1000)	Cell Signaling Technologies	Cat# 4970 RRID:AB_2223172
Mouse anti-MLH1 (IF, 1:500)	BD Biosciences:	Cat# 551092 RRID:AB_394041
Mouse anti- γ H2AX (IF, 1:1000)	Abcam	Cat# ab26350 RRID:AB_470861
Rabbit anti-DMC1 (IF, 1:1000)	Santa Cruz	Cat# SC-22768 RRID:AB_2277191
Rabbit anti-RAD51 (IF, 1:500)	Santa Cruz	Cat# SC-8349 RRID:AB_2253533
Rabbit anti-MEIOB (IF, 1:100)	Millipore	Cat# ABE1414 RRID:AB_297813
Rabbit anti-SPATA22 (IF, 1:100)	Proteintech	Cat# 16989-1-AP RRID:AB_2286640
Rabbit anti-RPA1/RPA70 (IB, 1:1000)	Abcam	Cat# ab87272 RRID:AB_2180493
Rat anti-RPA2 (IF, 1:1000)	Cell Signaling Technologies	Cat# 2208 RRID:AB_2238543
Rabbit anti-SYCP1 (IF, 1:1000)	Abcam	Cat# ab15090 RRID:AB_301636
Goat anti-BRCA1(IF, 1:500)	Santa Cruz	Cat# SC-1553 RRID:AB_2067340
Rabbit anti-BRCA2 (IB, 1:1000)	Abcam	Cat#, ab27976 RRID:AB_2067760
Guinea pig anti-SYCP3 (IF, 1:2000)	Ishiguro et al., 2020	N/A
Rat anti-SYCP3(IF, 1:1000)	Ishiguro et al., 2020	N/A
Mouse anti-mouse SYCP1 (IF, 1:1000)	Ishiguro et al., 2011	N/A
Guinea pig anti-H1t (IF, 1:2000)	provided by Marry Ann Handel	N/A
Rabbit anti-MEILB2/HSF2BP (WB, 1:1000)	This paper	N/A
Rat anti-MEILB2/HSF2BP (IF, 1:500)	This paper	N/A
Rat anti-mouse BRME1/MRM/4930432K21Rik/ C19orf57 (IF, 1:1000, WB, 1:1000, IP, 2 μ g per IP of testes extract)	This paper	N/A
Rabbit anti-mouse BRME1/MRM/4930432K21Rik/ C19orf57 (WB, 1:1000)	This paper	N/A
Bacterial and Virus Strains		
<i>E. coli</i> strain BL21-CodonPlus(DE3)-RIPL	Agilent	Cat# 230280
Chemicals, Peptides, and Recombinant Proteins		
Ni-NTA agarose	QIAGEN	Cat# 30210
Tissue-Tek O.C.T. compound	Sakura Finetek	Cat# 4583
Vectashield mounting medium containing DAPI	Vector Laboratory	Cat# H-1200
Superscript III Reverse Transcriptase	Thermo Fisher Scientific	Cat# 18080044
TRIzol reagent	Thermo Fisher Scientific	Cat# 15596018
Ex-Taq polymerase	Takara	Cat# RR001B
ECL prime	GE healthcare	Cat# RPN2232
NuPAGE 4-12%Bis-Tris Protein Gel	Thermo-Fisher Scientific	Cat# NP0322
CNBr-activated Sepharose	GE healthcare	Cat# 17043001
Dynabeads Protein A	Thermo-Fisher Scientific	Cat# 10002D
Dimethyl pimelimidate dihydrochloride (DMP)	Sigma-Aldrich	Cat# D8388
SimplyBlue	Thermo-Fisher	Cat# LC6065
Pierce DTT, No-Weight Format (48x7.7mg)	Thermo Fisher Scientific	Cat# 20291
Pierce Iodoacetamide, Single-Use (24x9.3mg)	Thermo Fisher Scientific	Cat# 90034
Trypsin/Lys-C Mix, Mass Spec Grad (5x20 μ g)	Promega	Cat# V5073
cOmplete, EDTA-free	Roche	Cat# 4 693 132
RIPA buffer	Thermo	Cat# 89900
collagenase	Sigma-Aldrich	Cat# C0130

(Continued on next page)

Continued

REAGENT or RESOURCE	SOURCE	IDENTIFIER
DNase II	Sigma-Aldrich	Cat# 8764
Proteinase inhibitor cocktail	Sigma-Aldrich	Cat# P8340
H&E Staining System	Leica	Cat# 3801698
Cas9 protein	NIPPON GENE	Cat# 317-08441
Glycogen	Wako	Cat# 077-05311
Triton X-100	Sigma-Aldrich	Cat# T9284
Opti-MEM I Reduced Serum Medium	Thermo Fisher Scientific	Cat# 31985062
RNasin® Plus Ribonuclease Inhibitors	Promega	Cat# N2611
Alexa Fluor 555 Antibody labeling kit	Thermo Fisher Scientific	Cat# A20187
Critical Commercial Assays		
MEBSTAIN Apoptosis TUNEL Kit Direct	MBL	Cat# 8445
TB Green Premix Ex TaqII (Tli RNaseH Plus)	Takara	Cat# RR820A
Deposited Data		
ChIP-seq of MEIOSIN and STRA8	Ishiguro et al., 2020	DDBJ DRA007778 DRA009056
Experimental Models: Organisms/Strains		
Mouse: <i>Brme1/Mrm/4930432K21rik</i> knockout	This paper	N/A
Mouse: <i>Spo11</i> knockout	Baudat et al., 2000	N/A
Mouse: C57BL/6N	SLC	N/A
Oligonucleotides		
tracrRNA	FASMAC	GE-002
Primers for RT-PCR, genotyping, genome editing	See Table S1	N/A
Recombinant DNA		
pET28c- <i>Brme1/Mrm/4930432K21Rik</i> -N	This paper	N/A
pET28c - <i>Meilb2</i>	This paper	N/A
Software and Algorithms		
genome browser IGV	Thorvaldsdottir et al., 2013	http://meme-suite.org/tools/meme-chip
SoftWorx	GE Healthcare	N/A
CellSens	OLYMPUS	N/A
BZ-X	KEYENCE	N/A
LASX ver.2	Leica	N/A
Proteome Discoverer version 1.4	Thermo Fisher Scientific	N/A
Mascot search engine version 2.5	Matrix Science	N/A
Xcalibur	Thermo Fisher Scientific	N/A
Thermal Cycler Dice Real Time System Software	Takara	Ver.5.11B for TP850
FlowJo version 10.0.7	Becton, Dickinson	RRID:SCR_008520
Prism8	Graphpad	RRID:SCR_002798
GEPIA2	Tang et al., 2017	http://gepia2.cancer-pku.cn/#index

RESOURCE AVAILABILITY

Lead Contact

Further information and requests for resources and reagents should be directed to and will be fulfilled by the Lead Contact, Kei-ichiro Ishiguro (ishiguro@kumamoto-u.ac.jp).

Materials Availability

4930432K21Rik knockout mouse lines generated in this study have been deposited to Center for Animal Resources and Development (CARD, ID 2775, 2776). The antibodies are available upon request. There are restrictions to the availability of antibodies due

to the lack of an external centralized repository for its distribution and our need to maintain the stock. We are glad to share antibodies with reasonable compensation by requestor for its processing and shipping. All unique/stable reagents generated in this study are available from the Lead Contact with a completed Materials Transfer Agreement.

Data and Code Availability

All data supporting the conclusions are present in the paper and the supplementary materials. Original data are deposited in Mendeley Data (<https://dx.doi.org/10.17632/jimg95zkyx.1>). Sequencing data for the mouse homolog of *C19orf57/4930432K21Rik* gene was initially deposited in the National Center for Biotechnology Information-National Institutes of Health (NCBI-NIH) GenBank under accession numbers LC507101 as *Miotic recombination modulator (Mrm)*, and posted on preprint server bioRxiv (<https://www.biorxiv.org/content/10.1101/2020.02.14.950204v2>). Later, we accepted the nomenclature *Brme1* that was given to *4930432K21Rik*. Mouse lines generated in this study have been deposited to Center for Animal Resources and Development (CARD), *4930432K21Rik* mutant mouse #11 (ID 2775) and *4930432K21Rik* mutant mouse #6 (ID 2776).

EXPERIMENTAL MODEL AND SUBJECT DETAILS

Animals

4930432K21Rik/Brme1 knockout mice were C57BL/6 background. *Spo11* KO knockout mouse was reported earlier (Baudat et al., 2000). Male mice were used for immunoprecipitation of testis extracts, histological analysis of testes, immunostaining of testes, RT-PCR experiments. Female mice were used for histological analysis of the ovaries, immunostaining experiments. Whenever possible, each knockout animal was compared to littermates or age-matched non-littermates from the same colony, unless otherwise described. Animal experiments were approved by the Institutional Animal Care and Use Committee (approval F28-078, A2020-006, A30-001, A28-026).

METHOD DETAILS

Generation of *4930432K21Rik/Brme1* knockout mice and genotyping

4930432K21Rik knockout mouse was generated by introducing Cas9 protein (317-08441; NIPPON GENE, Toyama, Japan), tracrRNA (GE-002; FASMAC, Kanagawa, Japan), synthetic crRNA (FASMAC), and ssODN into C57BL/6N fertilized eggs using electroporation. For generating *4930432K21Rik/Brme1* Exon3-9 deletion (Ex3-9Δ) allele, the synthetic crRNAs were designed to direct GCAGGAAGTTCATAGCCACA(ggg) of the *4930432K21Rik* intron 2 and TGGGTAACAGATCTACACAC(agg) in the 3'-neighboring region of the Exon9. ssODN: 5'-GGCTACAACACTACAGGGAGGTTTGTGCTCTCTAACCTGTGaattcGGCTATGAACCTCCTGCCGC CATCAGCTTCCAAAATACAG-3' was used as a homologous recombination template.

The electroporation solutions contained [10 μM of tracrRNA, 10 μM of synthetic crRNA, 0.1 μg/μl of Cas9 protein, ssODN (1 μg/μl)] for *4930432K21Rik* knockout in Opti-MEM I Reduced Serum Medium (31985062; Thermo Fisher Scientific). Electroporation was carried out using the Super Electroporator NEPA 21 (NEPA GENE, Chiba, Japan) on Glass Microslides with round wire electrodes, 1.0 mm gap (45-0104; BTX, Holliston, MA). Four steps of square pulses were applied (1, three times of 3 mS poring pulses with 97 mS intervals at 30 V; 2, three times of 3 mS polarity-changed poring pulses with 97 mS intervals at 30 V; 3, five times of 50 mS transfer pulses with 50 mS intervals at 4 V with 40% decay of voltage per each pulse; 4, five times of 50 mS polarity-changed transfer pulses with 50 mS intervals at 4 V with 40% decay of voltage per each pulse).

The targeted *4930432K21Rik* Ex3-9Δ allele in F0 mice were identified by PCR using the following primers; *4930432K21Rik*-1F: 5'-TGTTACACAAAGTCTTGAATCAG-3' and *4930432K21Rik*-3R: 5'-TCTGTGTGAGAATTGAGGCCTAAGC-3' for the knockout allele (309 bp). *4930432K21Rik*-2F: 5'-TAAATGATGCAGTCATGAGCCTCTG-3' and *4930432K21Rik*-1R: 5'-GGGGGTGATCAGAGC TCATTCTAG-3' for the Ex9 down stream of WT allele (345 bp). *4930432K21Rik*-1F and *4930432K21Rik*-2R: 5'-GGCTTTGAGG GATGGAGGCCGACCC-3': for the intron 2 of WT allele (365 bp). The PCR amplicons were verified by sequencing. Primer sequences are listed in Table S1.

PCR with reverse transcription

Total RNA was isolated from tissues and embryonic gonads using TRIzol (Thermo Fisher). cDNA was generated from total RNA using Superscript III (Thermo Fisher) followed by PCR amplification using Ex-Taq polymerase (Takara) and template cDNA.

For RT-qPCR, total RNA was isolated from WT, *Meiosin* KO and *Stra8* KO testes, and cDNA was generated as described previously (Ishiguro et al., 2020). *4930432K21Rik / Brme1* cDNA was quantified by ΔCT method using TB Green Premix Ex TaqII (Tli RNaseH Plus) and Thermal cycler Dice (Takara), and normalized by *GAPDH* expression level.

Sequences of primers used for RT-PCR (Figure 1A) are as follows:

GAPDH-F: 5'-TTCACCACCATGGAGAAGGC-3'
GAPDH-R: 5'-GGCATGGACTGTGGTCATGA-3'
4930432K21Rik-F1: 5'-GGCGACCTATTCCCCATCAG-3'
4930432K21Rik-R1: 5'-GGCCTTGTTCCTGGGAAGG-3'

Sequences of primers used for RT-PCR (Figure 1B; Figure S1B) are as follows:

4930432K21Rik qPCR-F: 5'- AGTCACCAAACCTCAATCCA-3'
4930432K21Rik qPCR-R: 5'- AACCCCTTTGTCAGGTAAGG-3'
Gapdh_F2: 5'-ACCACAGTCCATGCCATCAC-3'
Gapdh_R2: 5'-TCCACCACCCTGTTGCTGTA-3'

Primer sequences are listed in Table S1.

Preparation of testis extracts and immunoprecipitation

Testis chromatin-bound and -unbound extracts were prepared as described previously (Ishiguro et al., 2014). Briefly, testicular cells were suspended in low salt extraction buffer (20 mM Tris-HCl [pH 7.5], 100 mM KCl, 0.4 mM EDTA, 0.1% Triton X-100, 10% glycerol, 1 mM β -mercaptoethanol) supplemented with Complete Protease Inhibitor (Roche). After homogenization, the soluble chromatin-unbound fraction was separated after centrifugation at 100,000g for 10 min at 4°C. The chromatin bound fraction was extracted from the insoluble pellet by high salt extraction buffer (20 mM HEPES-KOH [pH 7.0], 400 mM KCl, 5 mM MgCl₂, 0.1% Tween20, 10% glycerol, 1 mM β -mercaptoethanol) supplemented with Complete Protease Inhibitor. The solubilized chromatin fraction was collected after centrifugation at 100,000g for 10 min at 4°C.

For immunoprecipitation of endogenous 4930432K21Rik from chromatin unbound fraction, 3.75 μ g of affinity-purified rat anti-4930432K21Rik and control IgG antibodies were crosslinked to 100 μ l of protein A-Dynabeads (Thermo-Fisher) by DMP (Sigma). The antibody-crosslinked beads were added to the testis extracts prepared from wild-type testes (17 to 21-day-old). The beads were washed with low salt extraction buffer. The bead-bound proteins were eluted with 40 μ l of elution buffer (100 mM Glycine-HCl [pH 2.5], 150 mM NaCl), and then neutralized with 4 μ l of 1 M Tris-HCl [pH 8.0]. The immunoprecipitated proteins were separately run on NuPAGE Bis-Tris 4%–12% gel (Thermo-Fisher) in MOPS-SDS buffer (Thermo-Fisher) for detection of BRME1, HSF2BP/MEILB, Actin, and on NuPAGE Tris-Acetate 3%–8% gel (Thermo-Fisher) in Tris-Acetate -SDS buffer (Thermo-Fisher) for detection of BRCA2, BRME1, HSF2BP/MEILB, RPA1, RAD51, DMC1, Actin. Immunoblots were detected by VeritBlot for IP detection reagent (HRP) (ab131366, abcam, 1:3000 dilution). Immunoblot image was developed using ECL prime (GE healthcare) and captured by FUSION Solo (VILBER). For the immunoblot of whole testes extracts from WT and *Brme1* KO mice, lysate were prepared in RIPA buffer and run on 8% Laemmli SDS-PAGE in Tris-Glycine-SDS buffer. Note that mobility of BRME1 protein was slower than expected molecular weight and slightly different depending on the gels and running buffers.

Mass spectrometry

The immunoprecipitated proteins were run on 4%–12% NuPAGE (Thermo Fisher) by 1 cm from the well and stained with SimplyBlue (Thermo Fisher) for the in-gel digestion. The gel containing proteins was excised, cut into approximately 1mm sized pieces. Proteins in the gel pieces were reduced with DTT (Thermo Fisher), alkylated with iodoacetamide (Thermo Fisher), and digested with trypsin and lysyl endopeptidase (Promega) in a buffer containing 40 mM ammonium bicarbonate, pH 8.0, overnight at 37°C. The resultant peptides were analyzed on an Advance UHPLC system (ABRME1ichrom Bioscience) coupled to a Q Exactive mass spectrometer (Thermo Fisher) processing the raw mass spectrum using Xcalibur (Thermo Fisher Scientific). The raw LC-MS/MS data was analyzed against the NCBI non-redundant protein/translated nucleotide database restricted to *Mus musculus* using Proteome Discoverer version 1.4 (Thermo Fisher) with the Mascot search engine version 2.5 (Matrix Science). A decoy database comprised of either randomized or reversed sequences in the target database was used for false discovery rate (FDR) estimation, and Percolator algorithm was used to evaluate false positives. Search results were filtered against 1% global FDR for high confidence level. All full lists of MSMS data are shown in Table S2 (Excel file).

Antibodies

The following antibodies were used for immunoblot (IB) and immunofluorescence (IF) studies: rabbit anti-Actin (IB, 1:1000, CST #4970), mouse anti-MLH1 (IF, 1:500, BD Biosciences: 551092), rabbit anti-SYCP1 (IF, 1:1000, Abcam ab15090), mouse anti- γ H2AX (IF, 1:1000, Abcam ab26350), rabbit anti-DMC1 (IF, 1:500, Santa Cruz: SC-22768), rabbit anti-RAD51 (IF, 1:500, Santa Cruz: SC-8349), rabbit anti-SPATA22 (IF, 1:100, proteintech 16989-1-AP), rabbit anti-RPA1/RPA70 (IB, 1:1000, Abcam ab87272), rat anti-RPA2 (IF, 1:1000, CST 2208), rabbit anti-MEIOB (IF, 1:100, Millipore # ABE1414), mouse anti-SYCP1 (IF, 1:1000) (Ishiguro et al., 2011), rat anti-SYCP3 (Ishiguro et al., 2020) (IF, 1:1000), guinea pig anti-SYCP3 (Ishiguro et al., 2020) (IF, 1:2000), goat anti-BRCA1 (IF, 1:500, SantaCruz sc-1553), rabbit anti-BRCA2 (IB, 1:1000, Abcam ab27976), guinea pig anti-H1t (IF, 1:2000, kindly provided by Marry Ann Handel).

Polyclonal antibodies against mouse BRME1/4930432K21Rik-N and mouse MEILB2/HSF2BP were generated by immunizing rabbits and rats. His-tagged recombinant proteins of BRME1/4930432K21Rik-N (aa 1-207) and MEILB2/HSF2BP (Full length) were produced by inserting cDNA fragments in-frame with pET28c (Novagen) in *E. coli* strain BL21-CodonPlus(DE3)-RIPL (Agilent), solubilized in a denaturing buffer (6 M HCl-Guanidine, 20 mM Tris-HCl [pH 7.5]) and purified by Ni-NTA (QIAGEN) under denaturing

conditions. The antibodies were affinity-purified from the immunized serum with immobilized antigen peptides on CNBr-activated Sepharose (GE healthcare). Rat MEILB2/HSF2BP antibody was labeled by Alexa555 using Alexa Fluor 555 Antibody labeling kit (Thermo A20187).

Histological Analysis

Testes, caudal epididymis and ovaries were fixed in Bouin's solution, and embedded in paraffin. Sections were prepared on CREST-coated slides (Matsunami) at 6 μ m thickness. The slides were dehydrated and stained with hematoxylin and eosin.

For Immunofluorescence staining, testes were embedded in Tissue-Tek O.C.T. compound (Sakura Finetek) and frozen. Cryosections were prepared on the CREST-coated slides (Matsunami) at 8 μ m thickness, and then air-dried. The serial sections of frozen testes were fixed in 4% paraformaldehyde in PBS for 5 min at room temperature and washed briefly in PBS. After washing, the serial sections were permeabilized in 0.1% Triton X-100 in PBS for 5 min. The sections were blocked in 3% BSA/PBS, and incubated at room temperature with the primary antibodies in a blocking solution. After three washes in PBS, the sections were incubated for 1 h at room temperature with Alexa-dye-conjugated secondary antibodies (1:1500; Invitrogen) in a blocking solution. TUNEL assay was performed using MEBSTAIN Apoptosis TUNEL Kit Direct (MBL 8445). DNA was counterstained with Vectashield mounting medium containing DAPI (Vector Laboratory).

Immunostaining of spermatocytes

Surface-spread nuclei from spermatocytes and oocytes were prepared by the dry down method as described (Peters et al., 1997) with a modification. The slides were then air-dried and washed with water containing 0.1% Tween20 or frozen for longer storage at -30°C . For staining of HSF2BP/MEILB2, the slides were heat-treated briefly by microwave oven in TE (pH8.0) for antigen retrieval. The slides were permeabilized in 0.1% Triton X-100 in PBS for 5 min, blocked in 3% BSA/PBS, and incubated at room temperature with the primary antibodies in 3% BSA/PBS. For immunostaining of SPATA22, slides were blocked in PBS containing 5% skim milk and 5% FBS. After three washes in PBS, the sections were incubated for 1 h at room temperature with Alexa-dye-conjugated secondary antibodies (1: 1500; Invitrogen) in a blocking solution. DNA was counterstained with Vectashield mounting medium containing DAPI (Vector Laboratory).

Imaging

Immunostaining images were captured with DeltaVision (GE Healthcare). The projection of the images was processed with the SoftWorx software program (GE Healthcare). All images shown were Z stacked. Bright field images were captured with OLYMPUS BX53 fluorescence microscope and processed with CellSens standard program. For counting seminiferous tubules, immunostaining images were captured with BIOREVO BZ-X710(KEYENCE), and processed with BZ-H3A program.

FACS analysis

Testes were scraped and digested with accutase (Innovative cell technologies Inc.) at room temperature in the presence of DNase II followed by filtration through a 40 μ m cell strainer (FALCON). The testicular cells were fixed in 70% ethanol for over night, washed twice with 1% BSA in PBS and brought to a concentration of 1×10^6 cells/ml in propidium iodide/RNase solution (50 μ g/mL). DNA content was analyzed using SP6800 spectral analyzer (Sony Biotechnology Inc., Tokyo, Japan) with 488nm laser illumination. Data were analyzed and processed using FlowJo for PC, version 10.0.7 (Becton, Dickinson & Company, Ashland, OR).

ChIP-seq Data and Public RNA-seq data Analysis

MEIOSIN and STRA8 ChIP-seq data were described in our previous study (Ishiguro et al., 2020), and analyzed for 4930432K21Rik / *Brme1* locus. MEIOSIN and STRA8 binding sites were shown along with genomic loci from Ensembl on the genome browser IGV.

Public RNA-seq data was analyzed using GEPIA2 server <http://gepia2.cancer-pku.cn/#index> (Tang et al., 2017) at the threshold of Log2FC Cutoff:1, p value Cutoff:0.01.

QUANTIFICATION AND STATISTICAL ANALYSIS

Statistical analysis was performed using GraphPad Prism or Microsoft EXCEL.

Figure 1A RT-PCR data was taken from an adult male (1 animal) and an adult female (1 animal).

Figure 1B RT-PCR data was taken from female embryos at indicated time points (one embryo for each time point).

Figure 1C Foci counting data was pooled from 3 males.

Figure 1D Data was acquired from *Spo11* KO male (1 animal).

Figure 2B BRME1 protein level was examined by western blotting from WT (P18; 2 animals), *Brme1* \pm (P18; 1 animal) and *Brme1* KO (P18; 2 animals).

Figure 2C Background signals of BRME1 immunostaining were counted at each stage from WT (1 animal) and *Brme1* KO (1 animal). n: the number of cells examined at each stage.

Figure 2D Quantification of a pair of testes/body-weight ratio (mg/g) in *Brme1* \pm (8w; n = 3) and *Brme1* KO (8w; n = 3) mice. n: the number of animals examined for each genotype. Bar graph indicates mean with SD. Statistical significance was determined by t test.

Figure 2E Quantification of the seminiferous tubules that have H1t +/SYCP3+ cells per the seminiferous tubules that have SYCP3+ spermatocyte cells in WT (p18: n = 4, 8w: n = 3), heterozygous (p18: n = 3, 8w: n = 4) and *Brme1* KO (p18: n = 3, 8w: n = 5) testes. n: the number of animals examined for each genotype. Bar graph indicates mean with SD. Statistical significance was determined by t test.

Figure 2F Spermatocytes in the four developmental stages (leptotene, zygotene, pachytene, and diplotene) per total cells in meiotic prophase were quantified in WT (n = 350 from one animal) and *Brme1* KO (n = 306 from one animal).

Figure 2I Numbers of MLH1 foci on SYCP3 axes were counted in WT and *Brme1* KO. Number of foci was indicated in the scatterplot with median. *p*-value (Mann-Whitney U-test) is shown.

Figure 2J Quantification of the TUNEL+ cells per total SYCP3 + spermatocytes in WT, *Brme1* ± and *Brme1* KO mice (P18). Percentages of TUNEL+ cells per total SYCP3 + spermatocytes were calculated in 16 seminiferous tubules, that have at least one TUNEL+ cell. Averaged percentage from 3 animals (total 48 tubules) for each genotype is calculated. Bar graph indicates mean with SD. Statistical significance was determined by t test.

Figure 2K Quantification of the seminiferous tubules that have TUNEL+ cells per total tubules in WT (8w: n = 3), *Brme1* ± (8w: n = 4) and *Brme1* KO (8w: n = 5) testes. Bar graph indicates mean with SD. Statistical significance was determined by t test.

Figure 3C Quantification of overlapped BRME1 and MEILB2 foci per total BRME1 or per total MEILB2 is shown (n = 10). Bar graph indicates mean with SD.

Figure 3D Quantification of overlapped BRME1 and MEIOB foci per total BRME1 or per total MEIOB is shown (n = 11). Bar graph indicates mean with SD.

Figure 3E Quantification of overlapped BRME1 and RDA51 foci per total BRME1 or per total RDA51 is shown (n = 15). Bar graph indicates mean with SD.

Figure 3F Quantification of overlapped BRME1 and DMC1 foci per total BRME1 or per total DMC1 is shown (n = 11). Bar graph indicates mean with SD.

Figures 4A–4F Numbers of MEIOB, RPA2, SPATA22, MEILB2, DMC1 and RAD51 foci on SYCP3 axes were counted in WT and *Brme1* KO. Number of foci was indicated in the scatterplot with median. *p*-value (Mann-Whitney U-test) is shown.

Figure S1B Testis RNA was obtained from P8 WT (3 animals), P10 WT (4 animals), *Meiosin* KO (3 animals) and *Stra8* KO (4 animals). qPCR was performed in triplicates, and the average ddCt values were calculated for individual cDNA samples. The expression level of *Brme1* was divided by that of *GAPDH* to give a relative expression level of *Brme1* to *GAPDH*. Relative expression level of *Brme1* to *GAPDH* was normalized to 1 for a given P10 WT sample. Bar graph indicates mean with SD. Statistical significance was determined by t test.

Figure S1C The boxplot was generated using GEPIA server (Tang et al., 2017). Red box indicates tumor. Grey box indicates normal tissue. The numbers of normal (num(N)) and tumor (num(T)) samples are indicated. Statistical significance was determined by one-way ANOVA.

Figure S3A Quantification of the seminiferous tubules containing post-meiotic cells per total number of the seminiferous tubules in WT (n = 3), *Brme1* ± (n = 4) and *Brme1* KO (n = 5) mice. Bar graph indicates mean with SD. Statistical significance was determined by t test.

Figure S3B Quantification of 1N post-meiotic cells from flow cytometry histogram were performed using Flowjo. Bar graph indicates mean with SD. Data was acquired from WT (8w; 3 animals), *Brme1* ± (8w; 3 animals) and *Brme1* KO (8w; 3 animals). Statistical significance was determined by t test.

Figure S4A Data was acquired from WT (1 animal) and *Brme1* KO female embryos (1 animal).

Figure S4B Adult ovaries examined by HE staining were acquired from *Brme1* ± (1 animal) and *Brme1* KO (2 animals) females.